Quantized Hall current in a topological nodal-line semimetal under electromagnetic waves

Po-Hsin Shih [1], Thi-Nga Do [2], Godfrey Gumbs,[1,3] Danhong Huang,[4,*] Hsin Lin,[5,†] and Tay-Rong Chang[2,6,7,‡]

[1]*Department of Physics and Astronomy, Hunter College of the City University of New York, 695 Park Avenue, New York, New York 10065, USA*
[2]*Department of Physics, National Cheng Kung University, Tainan 701, Taiwan*
[3]*Donostia International Physics Center (DIPC), P de Manuel Lardizabal, 4, 20018 San Sebastian, Basque Country, Spain*
[4]*US Air Force Research Laboratory, Space Vehicles Directorate (AFRL/RVSU), Kirtland Air Force Base,*
Albuquerque, New Mexico 87117, USA
[5]*Institute of Physics, Academia Sinica, Taipei 11529, Taiwan*
[6]*Center for Quantum Frontiers of Research and Technology (QFort), Tainan 701, Taiwan*
[7]*Physics Division, National Center for Theoretical Sciences, Taipei 10617, Taiwan*

Photocurrent acts as one of measurable responses of material to light, which has proved itself to be crucial for sensing and energy harvesting. Topological semimetals with gapless energy dispersion and abundant topological surface and bulk states exhibit exotic photocurrent responses, such as quantized circular photogalvanic effect observed in Weyl semimetals. Here we find that for a topological nodal-line semimetal with special ring bulk states and drumhead surface states (DSS), a significant photocurrent can be produced by an electromagnetic (EM) wave by means of the quantum Hall effect. The Hall current is enabled by electron transfer between Landau levels (LLs) and triggered by both the electric field and magnetic field components of an EM wave. This Hall current is physically connected to an unusually large quantum-Hall conductivity of the zeroth LLs resulting from quantized DSS. These LLs are found to be highly degenerate because of the unique band-folding effect associated with magnetic-field-induced expansion of a unit cell. We found that the Hall current generated solely by an in-plane linearly polarized EM wave is a quantized entity, regardless of its frequency and energy, which distinguishes it from the photocurrent observed thus far. This discovery opens up possibilities for Hall rectifiers and sensors, with potential industrial and space applications.

I. INTRODUCTION

The response of solids to external fields, such as photocurrent, has been a central topic in solid state physics. Photocurrent can be triggered by the photon absorption through various photoelectric effects like photovoltaic [1] and photogalvanic [2,3]. EM wave-induced quantum Hall effect (EMQHE) in the optical regime, known as optical QHE, has recently emerged as an alternative mechanism for the photocurrent generation. The optical Hall current is generated by the charge pumping in the magnetic-field-induced Landau levels (LLs) in the systems with finite Hall conductance [4–6]. Up to now, the quantum Hall plateaus in the terahertz (THz) regime have been investigated in a two-dimensional (2D) electron gas system [4] and graphene [5,6]. However, these optical QHE require an external magnetic field (***B***), in addition to an incident light. Though realization of optical QHE engendered entirely by EM wave can be enabled by the recent advanced development of the modern materials fabrication and THz light source technology, probing the optical QHE still remains challenging because the induced current response is relatively

weak and sensitive to the EM oscillation. Seeking materials with efficient EM wave-current conversion is highly desirable for sensing and energy harvesting.

Topological semimetals (TSM) are promising materials to engender exotic photocurrent because of their special topological surface and bulk states. TSM are characterized by band crossing in the Brillouin zone (BZ) at or in the vicinity of the Fermi level (E_F). The conventional TSM can be classified into three different categories, namely, Dirac semimetal, Weyl semimetal, and nodal-line semimetal (NLSM) [7]. The crossings of the bulk conduction and valence subbands of these systems form, respectively, the Dirac points [7–9], Weyl points [7–9], and 1D nodal lines [7,9–11] in the BZ. The TSM support unique surface states, which have been identified for the Fermi-arc surface states in Dirac semimetal [12] and Weyl semimetal [13], and drumhead surface states (DSS) in NLSM [14–16]. The photocurrent of TSM has been demonstrated unique, especially since the discovery of the quantized circular photogalvanic effect in WSM [3], for which the photocurrent depends only on fundamental constants and the monopole charge of a Weyl node.

Magnetic quantization is an important phenomenon, which could be exploited for achieving the essential understanding of the topological behaviors in materials. This feature in TSM has enabled the realization of the Dirac fermions [17–19] and the chiral anomaly in Dirac semimetal and Weyl

*Contact author: danhong.huang@us.af.mil
†Contact author: nilnish@gmail.com
‡Contact author: u32trc00@phys.ncku.edu.tw

semimetal [20–22]. Although the magnetic quantization of NLSM was previously predicted [23–26] and discovered [27], it has been limited to bulk or 1D ribbon LLs. Meanwhile the fully quantized DSS LLs, which could bear crucial topological fingerprints of the system, remain largely unknown. Magnetic quantization is the part of QHE that describes the high-order response to external $\boldsymbol{B}$ of a system. In general, a full theory of the electron response to high order in external fields can be established via the Berry curvature and a first-order correction to the band energy because of the orbital magnetic moment. The derivation of the second-order field correction to the Berry curvature of Bloch electrons in external EM fields [28] is essential for the study of response functions. So far, enormous attention has been devoted for the nonlinear effects of high-order electric field ($\boldsymbol{E}$), such as the nonlinear Hall effect in the absence of $\boldsymbol{B}$ up to second order [29,30] and third order [31]. Now, it is natural to ask if the high-order responses to both $\boldsymbol{B}$ and $\boldsymbol{E}$ can be addressed? And will it lead to any novel physical phenomena? Here, we answer these questions by presenting the EMQHE current of high-order $\boldsymbol{B}$ and $\boldsymbol{E}$ in NLSM.

The main achievements of this paper are threefold: (1) We observe the unique magnetic quantization phenomena of the NLSM DSS with unusually large, field-dependent surface quantum Hall conductivity (QHC) that have never been observed in the explored materials. By introducing a concept dealing with field-induced band folding, we uncover a fundamental understanding of the magnetic quantization mechanism in solids. We find that the degeneracies of LLs directly reflect the distribution of DSS within the folded BZ. (2) We derive semiclassically a general formula for the high-order current density and discover its relationship with the Berry curvature. This formula serves as an important basis for the investigation of photocurrent of materials. (3) We find a quantized signature in physics, which is the Hall current induced by an applied low-frequency linearly polarized EM field on the DSS. The current response can be determined by only the fundamental constants and area of DSS.

II. RESULTS AND DISCUSSION

We model the bulk NLSM by single atoms with two orbitals in the simple cubic unit cell, as seen in Fig. 1(a). The surface states can be formed in a slab containing multilayers along the [001] axis. Figure 1(b) shows the bulk BZ with high-symmetry points on the $k_z = 0$ plane [Γ, X, S, Y] and $k_z = \pi$ plane [Z, U, R, T] as well as the (001)-projected surface BZ. We assume that the system has spin degeneracy. The minimum tight-binding Hamiltonian (TBH) 2×2 matrix within the (s, p_z) basis for the bulk system can be written as

$$H = \begin{bmatrix} t(f_1 + f_2) + t_z f_3^+ + \epsilon_0 & t_{z'} f_3^- \\ -t_{z'} f_3^- & t(f_1 + f_2) + t_z f_3^+ - \epsilon_0 \end{bmatrix}.$$
(1)

In Eq. (1), $f_1 = e^{i\boldsymbol{k}\cdot\boldsymbol{r_1}} + e^{-i\boldsymbol{k}\cdot\boldsymbol{r_1}}$, $f_2 = e^{i\boldsymbol{k}\cdot\boldsymbol{r_2}} + e^{-i\boldsymbol{k}\cdot\boldsymbol{r_2}}$, and $f_3^\pm = e^{i\boldsymbol{k}\cdot\boldsymbol{r_3}} \pm e^{-i\boldsymbol{k}\cdot\boldsymbol{r_3}}$ are the phase terms with $\boldsymbol{k}$ the wave vector and $\boldsymbol{r_{1,2,3}}$ the unit vectors along x, y, z directions. The hopping integral $t = -2$ eV is for the horizontal interactions,
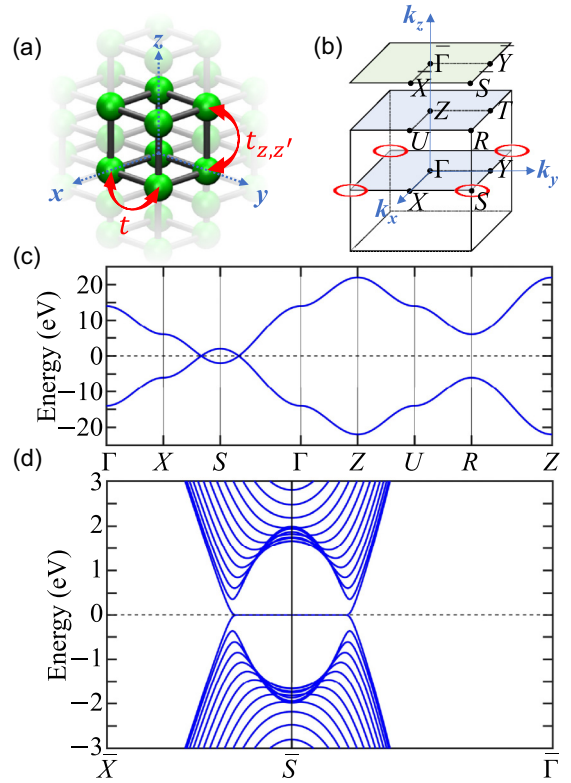

FIG. 1. (a) Crystal structure of a NLSM. (b) First BZ with high symmetry points for the bulk (lower) and slab (upper). For a 3D system, the first BZ is a cubic centered at Γ point, while it changes to a square centered at $\bar{\Gamma}$ for a 2D slab. The red circles indicate the Dirac nodal rings of energy bands. (c) Bulk band structure along the high symmetry points. (d) Band structure of a 25-layer slab consists of (001) surface bands at zero energy and nearby bulk bands.

while $t_z = 2$ eV and $t_{z'} = 1$ eV are for the interactions between the same and different orbital domains in the vertical direction, respectively. $\epsilon_0 = 10$ eV is the site energy.

The calculated bulk band structure along the high-symmetry points is shown in Fig. 1(c). The intersection of the conduction and valence bands forms a nodal ring encircling S on the $k_z = 0$ plane, giving the band crossing along the S-X and S-Γ directions in Fig. 1(c). On the contrary, the conduction and valence bands disperse apart elsewhere in the whole first BZ. The Dirac lines feature fourfold degeneracies, associated with the band crossing and equivalence between spin states. The slab band structure, shown in Fig. 1(d), consists of DSS around the $\bar{S}$ point and numerous highly dispersive bulk bands. The DSS are bounded by the projected nodal ring and almost dispersionless energy band. They are fourfold degenerate where both the electron and hole surface states coexist with spin degeneracy.

When a 2D condensed-matter system is subjected to a perpendicular $\boldsymbol{B}$ of $\boldsymbol{B} = (0,0,B)$, electrons follow quasiclassical cyclotron motion, thus electronic states are quantized into LLs. The application of $\boldsymbol{B}$ changes the lattice periodicity so that the primitive unit cell is extended along the x direction. Particularly, the field-induced Peierls phase of the form $G_R = (2\pi/\Phi_0)\int_R^r \boldsymbol{A} \cdot d\boldsymbol{\ell}$ needs to be included in the TBH [32]. Here, $\boldsymbol{A} = (0, Bx, 0)$ is the vector potential
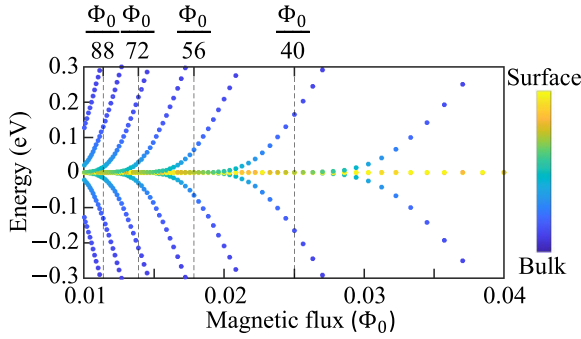
FIG. 2. The magnetic-flux-dependent LL energy spectrum for a 25-layer slab. The surface and bulk states are illustrated by yellow and blue dots, respectively. The surface spectral weights are defined as the states dominated by outer three layers of slab.

in the Landau gauge and $\Phi_0 = h/e$ is the flux quantum. The Peierls phases are repeated periodically along with the extended unit cell in the lattice when the total magnetic flux equals to Φ_0.

The Φ-dependent spectrum of DSS LLs is demonstrated in Fig. 2. $\Phi = B\mathcal{S}$ is the magnetic flux per unit cell with $\mathcal{S}$ being the area of the primitive unit cell in real space. We observe that the quantized LLs of DSS behaves similarly to the zeroth LLs of graphene and surface states of topological insulator. For these Dirac systems [17,33,34], it was previously shown that the flat zeroth LLs at the Dirac-point energy are independent of $\boldsymbol{B}$ strength. The LLs at higher energy, which arise from the linear band, acquire the square root dependence on both the LL index and the $\boldsymbol{B}$. For NLSM, the magnetic quantization of DSS yields a group of field-independent and nondispersive zeroth LLs, which only exist at $E_F = 0$. Note that, the surface LLs of NLSM are mainly produced from DSS, in contrast to the zeroth LLs of graphene and surface states of topological insulator, which are quantized partially from nearby states. With the increase of $\boldsymbol{B}$, the zeroth LLs gradually deform into bulk LLs at critical fields $\Phi_{N_L} = \frac{A_{DSS}}{A_{0,BZ}} \frac{\Phi_0}{N_L - 1/2}$, in which N_L is the number of degeneracies of the zeroth LLs and $A_{DSS}/A_{0,BZ}$ defines the ratio of the DSS area over the BZ area at zero $\boldsymbol{B}$. Consequently, the DSS LL degeneracies decrease by the number of peeled-off zeroth LLs. In fact, the surface LLs become highly degenerate only at low fields. This characteristic is unique for the DSS, which, to our knowledge, has never been observed in any other explored materials, and it plays a critical role in transport properties. The LLs merging mechanism can be understood well through the band-folding effect [35,36], which is accompanied by an enlarged real-space unit cell and a reduced size of the first BZ. Details about the relation between magnetic quantization and band folding can be found in Sec. I within the Supplemental Material [37] (see also Refs. [35,36] therein).

The probability function $|\psi|^2$, defined as the square of the magnitude of the wave function, is useful for identifying LLs. Figure 3(a) depicts $|\psi|^2$ for both surface and bulk LLs for $\Phi = \Phi_0/56$ on both α and β orbitals. Here, $|\psi|^2$ exhibits well-behaved oscillatory modes, and the number of zero nodes determines the corresponding LL index n. Since each pair of conduction and valence LLs acquires the same $|\psi|^2$, there are only four different oscillation modes, labeled
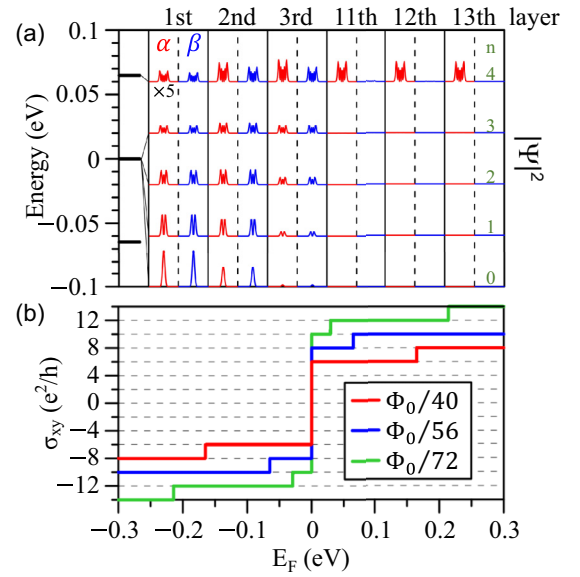

FIG. 3. (a) Selected spatial dependence of probability functions for LLs at low energies in a 25-layer slab. Here, α and β label two different orbitals. (b) E_F dependence of QHC at various instant Φ's.

by $n = 0, 1, 2, 3$ for the eightfold-degenerate zeroth LLs. Based on $|\psi|^2$ of the LLs at zero energy, it is clear that these modes are dominated by the outer three layers of the slab, i.e., they are the surface states. At higher energies, LLs (e.g., $n = 4$ LL) have nonvanishing $|\psi|^2$ on all layers, implying their bulk properties. Therefore, the distribution property of $|\psi|^2$ can be utilized to select out the surface LLs from bulk LLs in the system. This is considered as a key step in studying QHC of the DSS.

The QHE, one of the most essential electronic transport signatures for topological materials, exists a robust connection with magnetic quantization. The QHC is well quantized when E_F lies in the gap between two LLs and determined by the optical Hall conductivity [38]. In the limit of low frequency, the E_F-dependent QHC at the instant magnetic fields on the ideal NLSM system, shown in Fig. 3(b), can be calculated by employing the Kubo formula in the form (see Sec. II within the Supplemental Material [37]; see also Refs. [38–46] therein)

$$\sigma_{xy} = \frac{ie^2\hbar}{S} \sum_n \sum_{n' \neq n} (f_n - f_{n'}) \frac{\langle \Psi_n | \dot{u}_x | \Psi_{n'} \rangle \langle \Psi_{n'} | \dot{u}_y | \Psi_n \rangle}{(E_n - E_{n'})^2 + \Gamma_0^2}. \quad (2)$$

In this notation, E_n is the LL energy and $|\Psi_n\rangle$ is the corresponding nth-LL wave function. They are evaluated from the TBH in Eq. (1) and illustrated in Fig. 3(a). $\dot{u}_{x,y}$ are the velocity operators, f_n is the Fermi-Dirac distribution function, and Γ_0 (~ 1 meV) is the broadening factor. The calculated QHC displays the step features in which the plateaus correspond to vertical transition from occupied to unoccupied LLs. We found an unusually large QHC step for the zeroth LLs with high degeneracy via the relationship $\sigma_{xy} = C(e^2/h) = 2N_L(e^2/h)$, which implies the huge Chern number C as well as enormous Berry curvature. On the contrary, the steps of $2e^2/h$ are obtained for the bulk LLs because of the twofold spin degeneracy. Such substantial variation of the QHC at a
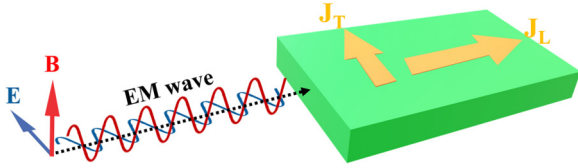
FIG. 4. Visual illustration of longitudinal (J_L) and transverse (J_T) currents in a NLSM under an EM field.

certain energy range has never been observed in the explored materials. For NLSM, the unique distribution of the DSS leads to the relation

$$N_L \cong \frac{A_{DSS}}{A_{B,BZ}} = \frac{A_{DSS}}{A_{0,BZ}} \frac{\Phi_0}{B\mathcal{S}},\tag{3}$$

in which $A_{B,BZ}$ is the folded BZ area under $\boldsymbol{B}$. This approximation is made within the limit of weak $\boldsymbol{B}$ (see Sec. I within the Supplemental Material [37]). In fact, the occupation of DSS in the first BZ can be manipulated by tuning the tight-binding parameters. Explicitly, by increasing the vertical hopping terms t_z and $t_{z'}$, the area of DSS is enhanced accordingly, leading to the change of critical fields for LLs merging and QHC steps. Our modeling and computations reveal similar features in band structure, LL spectra, and QHC at $E_F = 0$ for various sets of chosen parameters.

When a 2D system is subject to a linearly polarized EM field, there will occur a current across the material as a result of the QHE or photoelectric effects [1,3–6]. For the EMQHE, the high-order anomalous equilibrium (Berry-Hall) current component generated by Gaussian beam can be expressed semiclassically as (see Sec. III within the Supplemental Material [37]; see also references [28,47–54] therein)

$$\begin{aligned}
\boldsymbol{j}_1(t\,|\,E,B) = \frac{1}{\hbar} \int \frac{d^2\boldsymbol{k}}{(2\pi)^2} f_0\big[\varepsilon_n^{(0)}(\boldsymbol{k}\,|\,B) - \mu_e\big]\\
\times \big\{ \nabla_{\mathbf{k}}\big[\varepsilon_n^{(0)}(\boldsymbol{k}\,|\,B) + e\boldsymbol{E}(t) \cdot \boldsymbol{\mathcal{A}}_n^{(0)}(\boldsymbol{k}\,|\,B)\\
+ e\boldsymbol{E}(t) \cdot [\overleftrightarrow{\boldsymbol{\mathcal{G}}}_n^{(0)}(\boldsymbol{k}\,|\,B) \cdot \boldsymbol{E}(t)]\big]\\
+ e\boldsymbol{E}(t) \times \boldsymbol{\Omega}_n^{(0)}(\boldsymbol{k}\,|\,B)\\
+ e\boldsymbol{E}(t) \times [\nabla_{\mathbf{k}} \times \overleftrightarrow{\boldsymbol{\mathcal{G}}}_n^{(0)}(\boldsymbol{k}\,|\,B) \cdot \boldsymbol{E}(t)]\big\}.\tag{4}
\end{aligned}$$

Here, $\varepsilon_n^{(0)}(\boldsymbol{k}\,|\,B)$ represents the LL energies, $\overleftrightarrow{\boldsymbol{\mathcal{G}}}_n^{(0)}(\boldsymbol{k}\,|\,B)$ is the Berry-connection polarizability tensor, $\boldsymbol{\mathcal{A}}_n^{(0)}(\boldsymbol{k}\,|\,B)$ is the unperturbed Berry connection, and $\boldsymbol{\Omega}_n^{(0)}(\boldsymbol{k}\,|\,B)$ is the unperturbed Berry curvature of Bloch electrons. The anomalous thermal-equilibrium current includes both the parallel (J_L) and perpendicular (J_T) components respect to the direction of the EM field, referring to Fig. 4. They are associated with the quantized transverse conductivity and continuous longitudinal conductivity, for unique all-electron thermal-equilibrium transports. Note that both $\varepsilon_n^{(0)}(\boldsymbol{k}\,|\,B)$ and $\overleftrightarrow{\boldsymbol{\mathcal{G}}}_n^{(0)}(\boldsymbol{k}\,|\,B)$ are independent of k, thus the first and third and fifth terms are vanishing. The second term can not be physically observable since the Berry connection $\boldsymbol{\mathcal{A}}_n^{(0)}(\boldsymbol{k}\,|\,B)$ is a gauge-dependent variable. In general, the substantial $\boldsymbol{B}$-dependent Berry curvature $\boldsymbol{\Omega}_n^{(0)}(\boldsymbol{k}\,|\,B)$ plays the key role in determining the current response of the system. On the other hand, $\boldsymbol{\Omega}_n^{(0)}(\boldsymbol{k}\,|\,B)$ only has contribution to the longitudinal current. As a matter of fact,

the EMQHE current flowing in NLSM is dominated by $\boldsymbol{J}_L$, which can be written as (see Sec. III within the Supplemental Material [37])

$$\boldsymbol{J}_L(t) = \sigma_{xy}(t)E(t)\vec{n} \cong 2A_{DSS}v_0 e\vec{n}.\tag{5}$$

In this notation, $\vec{n}$ is the direction of the incident EM field. $v_0 = c/\sqrt{\epsilon}$ with ϵ being the dielectric function is a light speed in a dielectric medium. It is clear that at low frequency $\boldsymbol{J}_L$ depends only on the fundamental constants (e, h, c, Φ_0) and the intrinsic characteristics of the NLSM sample (see Sec. IV within the Supplemental Material [37]; see also Ref. [55] therein). In other words, the EMQHE current in NLSM is a quantized signature. Such a quantized entity originates from the unusually large DSS QHC, which distinguishes it from the previously discovered photocurrent. So far, the quantized current response has also been predicted in Weyl semimetal, in particular, the injection current depends only on the fundamental constants and the topological charge of Weyl nodes [3]. Such current is induced by the circular photogalvanic effect under a circularly polarized light. The condition for quantization of current response in WSM is the breaking of inversion and mirror symmetries, different from the time-reversal symmetry breaking in NLSM under EMQHE.

Ideally, a self-consistency current density of about $\frac{A_{DSS}}{A_{0,BZ}} \frac{ev_0}{\mathcal{S}}$ can be observed in NLSM when a suitable sample is placed under a low-frequency EM field (see Sec. V within the Supplemental Material [37]; see also Ref. [56] therein). This is up to five orders larger than that of graphene under the same condition [57]. Such topologically protected quantized Hall current will remain unchanged regardless of the incident in-plane linearly polarized EM field, as long as the DSS is quantized into LLs. From an application perspective, our unique results for the NLSM DSS can be put to technological applications and designing high-sensitivity detection devices (see Sec. VI within the Supplemental Material [37]; see also Refs. [49,58] therein). The significant and quantized Hall current is proper for designing new types of Hall rectifiers, which can convert EM waves into a direct and stable current. The robust connection between the current density and DSS enables the direct measurement of the density of DSS in topological NLSM. Furthermore, the strong dependence of the surface QHC on the $\boldsymbol{B}$ paves a way toward the development of $\boldsymbol{B}$-sensitive detectors for industrial and space applications. In particular, such a concise physics picture can be employed for developing AHE based compact and ultrasensitive magnetometers [59] in measuring a weak $\boldsymbol{B}$.

III. CONCLUSION

In conclusion, we have shown that the novel EMQHE current of the topological NLSM is a quantized response based on the novel magnetic quantization of DSS and its connection with field-induced band folding. We found the unusually large, field-dependent surface QHC induced by the extremely high LL degeneracy. We set an important groundwork for the study of photocurrent by deriving a general semiclassical formula for the high-order photocurrent. This paper has established a hallmark for studies of NLSM, which could play a critical role in next-generation technology and high-performance device applications.

[1] Y. Zhang, T. Holder, H. Ishizuka, F. de Juan, N. Nagaosa, C. Felser, and B. Yan, Switchable magnetic bulk photovoltaic effect in the two-dimensional magnet CrI3, Nat. Commun. **10**, 1 (2019).

[2] E. L. Ivchenko and S. D. Ganichev, Spin-photogalvanics, in *Spin Physics in Semiconductors*, edited by M. I. Dyakonov (Springer, Berlin, 2008), pp. 245-277.

[3] F. de Juan, A. G. Grushin, T. Morimoto, and J. E. Moore, Quantized circular photogalvanic effect in Weyl semimetals, Nat. Commun. **8**, 15995 (2017).

[4] Y. Ikebe, T. Morimoto, R. Masutomi, T. Okamoto, H. Aoki, and R. Shimano, Optical hall effect in the integer quantum Hall regime, Phys. Rev. Lett. **104**, 256802 (2010).

[5] R. Shimano, G. Yumoto, J. Y. Yoo, R. Matsunaga, S. Tanabe, H. Hibino, T. Morimoto, and H. Aoki, Quantum Faraday and Kerr rotations in graphene, Nat. Commun. **4**, 1841 (2013).

[6] H. Plank, M. V. Durnev, S. Candussio, J. Pernul, K.-M. Dantscher, E. Monch, A. Sandner, J. Eroms, D. Weiss, and V. V. Belkov, Edge currents driven by terahertz radiation in graphene in quantum Hall regime, 2D Mater. **6**, 011002 (2018).

[7] H. Weng, X. Dai, and Z. Fang, Topological semimetals predicted from first-principles calculations, J. Phys.: Condens. Matter **28**, 303001 (2016).

[8] N. P. Armitage, E. J. Mele, and A. Vishwanath, Weyl and Dirac semimetals in three-dimensional solids, Rev. Mod. Phys. **90**, 015001 (2018).

[9] H. Yang, A. Liang, C. Chen, C. Zhang, N. B. M. Schroeter, and Y. Chen, Visualizing electronic structures of quantum materials by angle-resolved photoemission spectroscopy, Nat. Rev. Mater. **3**, 341 (2018).

[10] T.-R. Chang, I. Pletikosic, T. Kong, G. Bian, A. Huang, J. Denlinger, S. K. Kushwaha, B. Sinkovic, H.-T. Jeng, T. Valla *et al.*, Realization of a type-II nodal-line semimetal in Mg_3Bi_2, Adv. Sci. **6**, 1800897 (2019).

[11] Y. K. Song, G. W. Wang, S. C. Li, W. L. Liu, X. L. Lu, Z. T. Liu, Z. J. Li, J. S. Wen, Z. P. Yin, Z. H. Liu, and D. W. Shen, Photoemission spectroscopic evidence for the Dirac nodal line in the monoclinic semimetal $SrAs_3$, Phys. Rev. Lett. **124**, 056402 (2020).

[12] S.-Y. Xu, C. Liu, S. K. Sushwaha, R. Sankar, J. W. Krizan, I. Belopolski, M. Neupane, G. Bian, N. Alidoust, T.-R. Chang *et al.*, Observation of Fermi arc surface states in a topological metal, Science **347**, 294 (2015).

[13] B. Q. Lv, H. M. Weng, B. B. Fu, X. P. Wang, H. Miao, J. Ma, P. Richard, X. C. Huang, L. X. Zhao, G. F. Chen *et al.*, Experimental discovery of Weyl semimetal TaAs, Phys. Rev. X **5**, 031013 (2015).

[14] M. M. Hosen, G. Dhakal, B. Wang, N. Poudel, K. Dimitri, F. Kabir, C. Sims, S. Regmi, K. Gofryk, D. Kaczorowski, A. Bansil, and M. Neupane, Experimental observation of drumhead surface states in $SrAs_3$, Sci. Rep. **10**, 2776 (2020).

[15] L. Muechler, A. Topp, R. Queiroz, M. Krivenkov, A. Varykhalov, J. Cano, C. R. Ast, and L. M. Schoop, Modular arithmetic with nodal lines: Drumhead surface states in ZrSiTe, Phys. Rev. X **10**, 011026 (2020).

[16] G. Bian, T.-R. Chang, H. Zheng, S. Velury, S.-Y. Xu, T. Neupert, C.-K. Chiu, S.-M. Huang, D. S. Sanchez, I. Belopolski, N. Alidoust, P.-J. Chen, G. Chang, A. Bansil, H.-T. Jeng, H. Lin, and M. Z. Hasan, Drumhead surface states and topological nodal-line fermions in $TlTaSe_2$, Phys. Rev. B **93**, 121113(R) (2016).

[17] Y.-S. Fu, M. Kawamura, K. Igarashi, H. Takagi, T. Hanaguri, and T. Sasagawa, Imaging the two-component nature of Dirac-Landau levels in the topological surface state of Bi_2Se_3, Nat. Phys. **10**, 815 (2014).

[18] V. M. Apalkov and T. Chakraborty, Interacting dirac fermions on a topological insulator in a magnetic field, Phys. Rev. Lett. **107**, 186801 (2011).

[19] P. Cheng, C. Song, T. Zhang, Y. Zhang, Y. Wang, J.-F. Jia, J. Wang, Y. Wang, B.-F. Zhu, X. Chen, X. Ma, K. He, L. Wang, X. Dai, Z. Fang, X. Xie, X.-L. Qi, C.-X. Liu, S.-C. Zhang, and Q.-K. Xue, Landau quantization of topological surface states in Bi_2Se_3, Phys. Rev. Lett. **105**, 076801 (2010).

[20] X. Yuan, Z. Yan, C. Song, M. Zhang, Z. Li, C. Zhang, Y. Liu, W. Wang, M. Zhao, Z. Lin *et al.* Chiral Landau levels in Weyl semimetal NbAs with multiple topological carriers, Nat. Commun. **9**, 1854 (2018).

[21] J. Xiong, S. K. Kushwaha, T. Liang, J. W. Krizan, M. Hirschberger, W. Wang, R. J. Cava, and N. P. Ong, Evidence for the chiral anomaly in the Dirac semimetal Na3Bi, Science **350**, 413 (2015).

[22] S. Jia, S.-Y. Xu, and M. Z. Hasan, Weyl semimetals, Fermi arcs and chiral anomalies, Nat. Mater. **15**, 1140 (2016).

[23] H. Yang, R. Moessner, and L.-K. Lim, Quantum oscillations in nodal line systems, Phys. Rev. B **97**, 165118 (2018).

[24] J.-W. Rhim and Y. B. Kim, Landau level quantization and almost flat modes in three-dimensional semimetals with nodal ring spectra, Phys. Rev. B **92**, 045126 (2015).

[25] K. Mullen, B. Uchoa, and D. T. Glatzhofer, Line of Dirac nodes in hyperhoneycomb lattices, Phys. Rev. Lett. **115**, 026403 (2015).

[26] G.-Q. Zhao, S. Li, W. B. Rui, C. M. Wang, H.-Z. Lu, and X. C. Xie, 3D quantum Hall effect in a topological nodal-ring semimetal, Quantum Front. **2**, 22 (2023).

[27] S. Li, Z. Guo, D. Fu, X.-C. Pan, J. Wang, K. Ran, S. Bao, Z. Ma, Z. Cai, R. Wang, R. Yu *et al.*, Evidence for a Dirac nodal-line semimetal in SrAs$_3$, Sci. Bull. **63**, 535 (2018).

[28] Y. Gao, S. A. Yang, and Q. Niu, Field induced positional shift of Bloch electrons and its dynamical implications, Phys. Rev. Lett. **112**, 166601 (2014).

[29] E. Deyo, L. E. Golub, E. L. Ivchenko, and B. Spivak, Semiclassical theory of the photogalvanic effect in non-centrosymmetric systems, arXiv:0904.1917v1.

[30] I. Sodemann and L. Fu, Quantum nonlinear Hall effect induced by berry curvature dipole in time-reversal invariant materials, Phys. Rev. Lett. **115**, 216806 (2015).

[31] S. Lai, H. Liu, Z. Zhang, J. Zhao, X. Feng, N. Wang, C. Tang, Y. Liu, K. S. Novoselov, S. A. Yang, and W.-B. Gao, Third-order nonlinear Hall effect induced by the Berry-connection polarizability tensor, Nat. Nanotechnol. **16**, 869 (2021).

[32] D. R. Hofstadter, Energy levels and wave functions of Bloch electrons in rational and irrational magnetic fields, Phys. Rev. B **14**, 2239 (1976).

[33] K. S. Novoselov, A. K. Geim, S. V. Morozov, D. Jiang, M. I. Katsnelson, I. V. Grigorieva, S. V. Dubonos, and A. A. Firsov, Two-dimensional gas of massless Dirac fermions in graphene, Nature (London) **438**, 197 (2005).

[34] V. P. Gusynin and S. G. Sharapov, Unconventional integer quantum Hall effect in graphene, Phys. Rev. Lett. **95**, 146801 (2005).

[35] A. Topp, R. Queiroz, A. Gruneis, L. Muchler, A. W. Rost, A. Varykhalov, D. Marchenko, M. Krivenkov, F. Rodolakis, J. L. McChesney, B. V. Lotsch, L. M. Schoop, and C. R. Ast, Surface floating 2D bands in layered nonsymmorphic semimetals: ZrSiS and related compounds, Phys. Rev. X **7**, 041073 (2017).

[36] B. I. Min and Y.-R. Jang, Band folding and Fermi surface in antiferromagnetic NdB$_6$, Phys. Rev. B **44**, 13270 (1991).

[37] See Supplemental Material at http://link.aps.org/supplemental/10.1103/PhysRevB.110.085427 for the magnetic quantization and band folding (Sec. I), ω-dependent optical Hall conductivity (Sec. II), the derivation of the anomalous equilibrium current (Sec. III), the quantization of the EMQHE current (Sec. IV), and application (Sec. V). A summary of each section is as follows. Section I: We seek a deep understanding for the magnetic quantization by connecting the LL degeneracy with field-induced band folding phenomenon. When the lattice periodicity is changed, the band folding occurs in momentum space. This is accompanied by an enlarged real-space unit cell and a reduced size of the first BZ. For the slab NLSM, such folding effect can be realized through variation of DSS occupation within the first BZ as a real-space unit cell expands in size. Section II: For the generation of LLs by an incident EM wave, besides the EM wave's frequency ω_0 being smaller than the LL separation to avoid inter-LL excitation, one also requires that the scatting rate $1/\tau_0$ of LLs should be smaller than the cyclotron frequency f_c to ensure that no mixing of different LLs occurs. Under these conditions, one can say that the electron dynamics can be viewed as ballistic transport in an ideal material. In the limit of $\omega \to 0$, the ω-dependent optical Hall conductivity equation leads to the frequently used expression for the dc QHE as Eq. (2). The consistency between the optical Hall conductivity and QHC at low frequency has been examined both experimentally and theoretically for various 2D materials. Section III: Based on the nonlinear dynamical theory for Boltzmann transport in 2D materials with geometric phases, we derived semiclassically the transient sheet-current density for non-adiabatic effects associated with the case for slowly varying external fields generated by Gaussian beam. We obtained both the anomalous equilibrium (Berry-Hall) current and the normal non-equilibrium (drifting and Lorentz-Hall) current. In our calculations, we include all effects of the external $\boldsymbol{B}(t)$ in the (zeroth-order) tight-binding band-structure and the effects of external $\boldsymbol{E}(t)$ up to the second-order perturbation. Then, the anomalous equilibrium current can be written as in Eq. (4). Section IV: For NLSM, the DSS area in the BZ presents a special relationship with the LL degeneracy, which can be observed through the band-folding effect. As a result, the LL degeneracy can be described by the areas of DSS, primitive unit cell, BZ, in addition to the magnetic field. Such unique characteristic of NLSM is responsible for the quantization of the EMQHE current. At low frequency, $\boldsymbol{J_L}$ depends only on the fundamental constants (e, h, c, Φ_0) and the intrinsic characteristics of the NLSM sample because the dielectric function ϵ is a constant.

[38] P. M. Oppeneer, in *Handbook of Magnetic Materials*, edited by K. H. J. Buschow (Elseveier, Amsterdam, 2001), Vol. 13, pp. 229–422.

[39] H. K. Avetissian and G. F. Mkrtchian, Coherent nonlinear optical response of graphene in the quantum Hall regime, Phys. Rev. B **94**, 045419 (2016).

[40] P. M. Krstajic and P. Vasilopoulos, Integral quantum Hall effect in graphene: Zero and finite Hall field, Phys. Rev. B **83**, 075427 (2011).

[41] A. Auerbach, I. Finkler, B. I. Halperin, and A. Yacoby, Steady states of a microwave-irradiated quantum-Hall gas, Phys. Rev. Lett. **94**, 196801 (2005).

[42] T. Oka and L. Bucciantini, Heterodyne Hall effect in a two-dimensional electron gas, Phys. Rev. B **94**, 155133 (2016).

[43] S. Kar and A. Saha, Fermi level fluctuations, reduced effective masses and Zeeman effect during quantum oscillations in nodal line semimetals, J. Phys.: Condens. Matter **34**, 035601 (2022).

[44] T. S. Seifert, U. Martens, F. Radu, M. Ribow, M. Berritta, L. Nadvornik, R. Starke, T. Jungwirth, M. Wolf, I. Radu *et al.*, Frequency-independent terahertz anomalous Hall effect in DyCo$_5$, Co$_{32}$Fe$_{68}$, and Gd$_{27}$Fe$_{73}$ thin films from DC to 40 THz, Adv. Mater. **33**, 2007398 (2021).

[45] Y. D. Kato, Y. Okamura, S. Minami, R. Fujimura, M. Mogi, R. Yoshimi, A. Tsukazaki, K. S. Takahashi, M. Kawasaki, R. Arita *et al.*, Optical anomalous Hall effect enhanced by flat bands in ferromagnetic van der Waals semimetal, npj Quantum Mater. **7**, 73 (2022).

[46] L. Galletti, A. Rashidi, D. A. Kealhofer, M. Goyal, B. Guo, Y. Li, C. Shang, J. E. Bowers, and S. Stemmer, Quantum Hall effect of the topological insulator state of cadmium arsenide in Corbino geometry, Appl. Phys. Lett. **118**, 261901 (2021).

[47] Q. Niu, M.-C. Chang, B. Wu, D. Xiao, and R. Cheng, *Physical Effects of Geometric Phases* (World Scientific, Singapore, 2017).

[48] D. Xiao, J. Shi, and Q. Niu, Berry phase correction to electron density of states in solids, Phys. Rev. Lett. **95**, 137204 (2005).

[49] H. Isobe, S.-Y. Xu, and L. Fu, High-frequency rectification via chiral Bloch electrons, Sci. Adv. **6**, eaay2497 (2020).

[50] L. E. Reichl, *A modern Course in Statistical Physics*, 4th ed. (Wiley-VCH, Weinheim, Germany, 2016).

[51] D. H. Huang, A. Iurov, H.-Y. Xu, Y.-C. Lai, and G. Gumbs, Interplay of Lorentz-Berry forces in position-momentum spaces for valley-dependent impurity scattering in α-T$_3$ lattices, Phys. Rev. B **99**, 245412 (2019).

[52] J. R. Gulley and D. Huang, Ultrafast transverse and longitudinal response of laser-excited quantum wires, Opt. Express **30**, 9348 (2022).

[53] J. C. Diels and W. Rudolph, *Ultrashort Laser Pulse Phenomenon: Fundamentals, Techniques, and Applications on a Femtosecond Time Scale* (Academic Press, new York, 2006).

[54] For cyclotron motion of electrons, one can estimate the time required for the quantization of continuous electronic states into discrete LLs from the cyclotron-resonance frequency $f = \frac{eB}{2\pi m^*}$ with an effective mass m^* for electrons. As $B = 0.1$T, we find $f \sim 2.8 \times 10^9$ Hz. For the generation of LLs by an incident electromagnetic wave, besides the EM wave's frequency ω_0 being smaller than the LL separation to avoid inter-LL excitation, one also requires that the scatting rate $1/\tau_0$ of LLs should be smaller than the cyclotron frequency f to ensure that no mixing of different LLs occurs. Under these conditions, one can say that the electron dynamics reflected in Eq. (5) can be viewed as ballistic transport in an ideal material.

[55] K. W.-K. Shung, Dielectric function and plasmon structure of stage-1 intercalated graphite, Phys. Rev. B **34**, 979 (1986).

[56] J. R. Gulley and D. Huang, Self-consistent quantum-kinetic theory for interplay between pulsed-laser excitation and nonlinear carrier transport in a quantum-wire array, Opt. Express OE **27**, 17154 (2019).

[57] S. D. Ganichev, D. Weiss, and J. Eroms, Terahertz electric field driven electric currents and ratchet effects in graphene, Ann. Phys. (NY) **529**, 1600406 (2017).

[58] S. Wu, Z. Zhang, K. Watanabe, T. Taniguchi, and E. Y. Andrei, Chern Insulators, van Hove singularities and topological flat bands in magic-angle twisted bilayer graphene, Nat. Mater. **20**, 488 (2021).

[59] Y. Zhang, K. Wang, and G. Xiao, Noise characterization of ultrasensitive anomalous Hall effect sensors based on $Co_{40}Fe_{40}B_{20}$ thin films with compensated in-plane and perpendicular magnetic anisotropies, Appl. Phys. Lett. **116**, 212404 (2021).